ARTICLES
https://doi.org/10.1038/s41561-020-0622-1
nature geoscience

A nutrient control on marine anoxia during the end-Permian mass extinction

Martin Schobben[1,2,7]✉, William J. Foster[2,3,8], Arve R. N. Sleveland[4], Valentin Zuchuat[4], Henrik H. Svensen[4], Sverre Planke[4], David P. G. Bond[5], Fons Marcelis[6], Robert J. Newton[1], Paul B. Wignall[1] and Simon W. Poulton[1]

Oxygen deprivation and hydrogen sulfide toxicity are considered potent kill mechanisms during the mass extinction just before the Permian–Triassic boundary (~251.9 million years ago). However, the mechanism that drove vast stretches of the ocean to an anoxic state is unclear. Here, we present palaeoredox and phosphorus speciation data for a marine bathymetric transect from Svalbard. This shows that, before the extinction, enhanced weathering driven by Siberian Traps volcanism increased the influx of phosphorus, thus enhancing marine primary productivity and oxygen depletion in proximal shelf settings. However, this non-sulfidic state efficiently sequestered phosphorus in the sediment in association with iron minerals, thus restricting the intensity and spatial extent of oxygen-depleted waters. The collapse of vegetation on land immediately before the marine extinction changed the relative weathering influx of iron and sulfate. The resulting transition to euxinic (sulfidic) conditions led to enhanced remobilization of bioavailable phosphorus, initiating a feedback that caused the spread of anoxic waters across large portions of the shelf. This reconciles a lag of >0.3 million years between the onset of enhanced weathering and the development of widespread, but geographically variable, ocean anoxia, with major implications for extinction selectivity.

The Permian–Triassic (P–Tr) boundary (~251.9 million years ago[1]) record contains multiple signals suggestive of widespread marine anoxia, a kill mechanism widely implicated in the end-Permian mass extinction[2–7]. This crisis was the most dramatic turning point in the evolution of post-Cambrian life, with a loss of up to 81% of marine species[8]. Mechanisms for the development of oxygen-depleted oceans on timescales compatible with the duration of the extinction (~60 kyr (ref. [1])), include changes in ocean circulation[9], decreased O_2 solubility under globally rising temperatures[10], and enhanced eutrophication[10–13]. In the latter case, recent studies have postulated that changes in the marine inventory of phosphorus (P)—the ultimate limiting nutrient for marine productivity on geological timescales[14]—was the main driver for eutrophication-induced oxygen depletion and ultimately the development of euxinic conditions in extensive regions of the global ocean[10,11,13].

During Siberian Traps volcanism, an increase in bioavailable phosphorus would be an expected consequence of increased continental weathering via the dissolution of exposed rock (driven by CO_2-induced warming and SO_2-induced acid rain) and the disintegration of rock by an invigorated hydrological cycle[11,12,15,16]. Indeed, a coeval change in both lithium (Li) concentrations and Li isotope ratios has been interpreted to reflect an increase in weathering[16]. Subsequently, a change in eruption style to intrusive basalt emplacement has been linked to halocarbon remobilization and exhalations leading to ozone-layer depletion and consequent terrestrial plant extirpations by ultraviolet-B irradiance[17,18]. The effects of this intrusive volcanic phase on land-plant communities have therefore been related to reduced soil stability[12,15,19]. Combined with continued greenhouse-induced global warming, and associated changes in the hydrological cycle, this situation probably led to increased soil erosion and physical weathering, thereby loading near-shore environments with a higher sediment influx and terrestrial organics[4,7,12,15].

Certain aspects of this scenario are problematic, as Siberian Traps activity spans >1 Myr, with two-thirds of the volume of lava deposited ~0.3 Myr before the main extinction pulse[18]. Furthermore, localized regions of dysoxia/anoxia occur before the mass extinction[3,4,6], but a major expansion in the areal extent of these conditions occurred at the extinction horizon[5,7]. The role of these precursor environmental changes in pre-stressed communities is underexplored[20] and requires knowledge of the mechanisms that drove the initiation of localized oxygen depletion and the ensuing expansion of anoxic regions.

While an increase in the oceanic influx of bioavailable phosphorus may have occurred in association with Siberian Traps activity[11,16], the catalytic effect of local redox conditions on benthic phosphorus remobilization has often been overlooked in scenarios of eutrophication-induced marine anoxia. Phosphorus is delivered to sediments in the form of organic matter and skeletal remains (biogenic apatite), as well as in association with iron (Fe) (oxyhydr) oxides and recalcitrant detrital minerals[21–24]. Organically bound P (P_{org}) may be preferentially released to sediment porewaters upon microbial remineralization, resulting in increased organic carbon (C_{org})/P_{org} ratios in deposited sediments[21,22]. In addition, the reductive dissolution of Fe (oxyhydr)oxides releases adsorbed P to solution[21–23], while biogenic apatite tends to be highly soluble[24].

The dissolved P generated by these processes may undergo 'sink-switching', whereby, dependent on the precise conditions, dissolved P may precipitate as either carbonate fluorapatite (CFA)[25] or Fe phosphates (for example, vivianite)[26], or may be readsorbed

[1]School of Earth and Environment, University of Leeds, Leeds, UK. [2]Museum für Naturkunde, Leibniz Institute for Research on Evolution and Biodiversity, Berlin, Germany. [3]Institute of Geosciences, Universität Potsdam, Potsdam, Germany. [4]Centre for Earth Evolution and Dynamics (CEED), Department of Geosciences, University of Oslo, Oslo, Norway. [5]Department of Geography, Geology and Environment, University of Hull, Hull, UK. [6]Shell Global Solutions International B.V., Amsterdam, Netherlands. [7]Present address: Department of Earth Sciences, Utrecht University, Utrecht, Netherlands. [8]Present address: School of Earth Sciences, University College Dublin, Dublin, Ireland. ✉e-mail: m.a.n.schobben@uu.nl

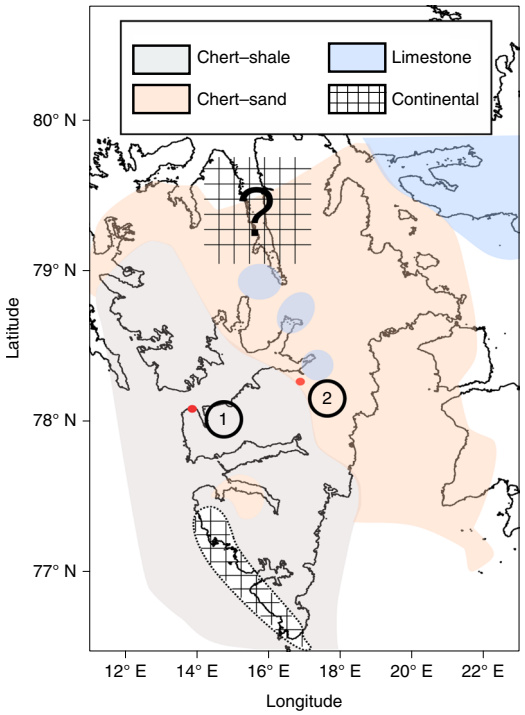

Fig. 1 | Geographical setting of the Festningen section and Deltadalen core. Late Permian lithofacies of Svalbard after ref. [29] and section 2 of the Supplementary Information. The tentative location of a northern source area (possibly on the Nordfjorden High) is demarcated with a question mark; the Sørkapp-Hornsund High is encircled with a dotted line. The red dots mark the exact locations of the Festningen section (1) and Deltadalen core (2). Base map from GADM database (https://gadm.org/).

to Fe (oxyhydr)oxides where such minerals persist[23]. However, under sulfidic conditions in particular, a substantial proportion of the dissolved P generated during early diagenesis may be recycled back to the water column, thus promoting a positive productivity feedback[27]. By contrast, organic-rich oxic, dysoxic and ferruginous (anoxic Fe(II)-rich) settings are potential loci of high P deposition. These features of phosphorus cycling thus place important constraints on the bioavailability of P and hence may ultimately control both the spread of anoxia and the generation of toxic dissolved hydrogen sulfide[11,27,28].

Previous attempts to reconstruct phosphorus availability[13] across the P–Tr transition have lacked a precise reconstruction of ocean redox conditions and detailed consideration of the phase partitioning of P, which are essential to evaluate the role of the P recycling feedback. To address this, we apply new sedimentary P records combined with independent redox proxies to a bathymetric transect across the P–Tr boundary.

Geological setting and materials

We investigated the Festningen and Deltadalen sequences (Svalbard; Fig. 1), which were deposited on a shallow, open-marine shelf at the northern margin of Pangaea, facing the Boreal Sea and the Panthalassa Ocean beyond (Supplementary Fig. 1 and sections 1–4 of the Supplementary Information). The Kapp Starostin Formation consists of dark, massive to bedded spiculitic chert (with minor shale) at Festningen[6,29], and glauconitic, fine-grained sandstone with chert nodules and beds at Deltadalen, where the latter is interpreted to be a comparatively more-proximal facies[6,30,31]. The Kapp Starostin Formation is overlain by the shale-dominated Vardebukta Formation at Festningen and by the Vikinghøgda Formation at Deltadalen.

The end-Permian mass extinction has been defined by a loss of intense bioturbation dominated by *Zoophycos*[4,6]. However, shallow bioturbation, dominated by small *Planolites*, persists for ~3 m above the formational contact at Festningen before disappearing[2]. The P–Tr boundary is defined with the aid of the $\delta^{13}C_{org}$ record (Fig. 2 and Supplementary Fig. 2) and the conodont marker species *Hindeodus parvus*[31].

Local redox chemistry

We combined iron speciation analyses with redox-sensitive trace element concentrations (Methods) to differentiate oxic, dysoxic, anoxic ferruginous and euxinic water-column conditions[32,33]. The Fe speciation method relies on the quantification of operationally defined Fe fractions that are considered highly reactive (Fe_{HR}) towards dissolved sulfide on early diagenetic timescales[34,35]. The proportion of Fe_{HR} relative to total iron (Fe_{tot}) has been extensively calibrated in modern and ancient settings, such that $Fe_{HR}/Fe_{tot} > 0.38$ suggests an anoxic water column, values below 0.22 indicate oxic depositional conditions and values of 0.22–0.38 are considered equivocal[36]. The extent of pyritization of Fe_{HR} is used to differentiate euxinic ($Fe_{py}/Fe_{HR} > 0.7$–0.8) from ferruginous water-column conditions ($Fe_{py}/Fe_{HR} < 0.7$) (ref. [36]).

Non-sulfidized Fe_{HR} has the potential to be converted to less-reactive sheet silicate minerals (termed poorly reactive sheet silicate Fe; Fe_{PRS}) during early diagenesis and deeper burial[35,37,38]. Depletion of Fe_{HR} by this mechanism is clearly observed in some of the studied samples and is marked by the co-occurrence of glauconite at both localities. Glauconite occurs as fibroradiated precipitates covering quartz grains and shell fragments, suggesting an authigenic precipitate rather than a late diagenetic replacement product or detrital source, and thus Fe_{HR} minerals would have been the primary source. To compensate for this transfer of Fe_{HR} to glauconite, we apply a correction to samples that show clear enrichment in Fe_{PRS} over background values, yielding estimates (Fe_{HR}/Fe_{tot}*, Fe_{py}/Fe_{HR}*) of initial depositional ratios[39] (Fig. 2, Supplementary Figs. 3 and 6 and section 7.2 of the Supplementary Information).

The distinctive geochemical behaviours of molybdenum (Mo), uranium (U) and rhenium (Re) provide further insight into water-column redox conditions. High sediment Mo accumulation tends to occur when water-column concentrations of sulfide are high and probably relates to the formation of particle-reactive thiomolybdates[33]. By contrast, U may be fixed in the sediment under anoxic porewater conditions, without the requirement for free H_2S, and Re may be sequestered under dysoxic conditions in the water column and sediments, where O_2 penetrates <1 cm below the sediment–water interface[33,40]. Therefore, high Re/Mo ratios tend to indicate dysoxic water-column conditions[40], whereas enhanced Mo/U ratios suggest a euxinic water column[33].

The pre-extinction sandstone of the proximal Deltadalen locality is conspicuous for its authigenic glauconite content. Glauconite formation is favoured by elevated concentrations of Fe_{HR}, silica and potassium under dysoxic conditions[41,42]. High Re/Mo ratios across this interval (Fig. 2)[40] coupled with the ichnoassemblage and the impoverished shelly faunal record, which consists of the inarticulate brachiopod *Lingularia freboldi*[43,44] (Supplementary Figs. 4 and 5 and section 7.1 of the Supplementary Information), are consistent with prevailing dysoxic seafloor conditions. Thus, the elevated Fe_{HR}/Fe_{tot}* values of the Kapp Starostin Formation (Fig. 2) probably reflect the influx of a high proportion of Fe (oxyhydr)oxides produced during enhanced weathering[35], rather than anoxic water-column conditions.

Enrichments in Re begin to decrease below the extinction interval at Deltadalen, coincident with increasing Mo/U ratios (Fig. 2). These high ratios coincide with enhanced fixation of Fe_{HR} as pyrite (Fig. 2), Mo_{EF}/U_{EF} that approach those observed in modern euxinic settings (Fig. 3) and the disappearance of burrows (Supplementary Fig. 2), suggesting the development of dominantly euxinic conditions in the

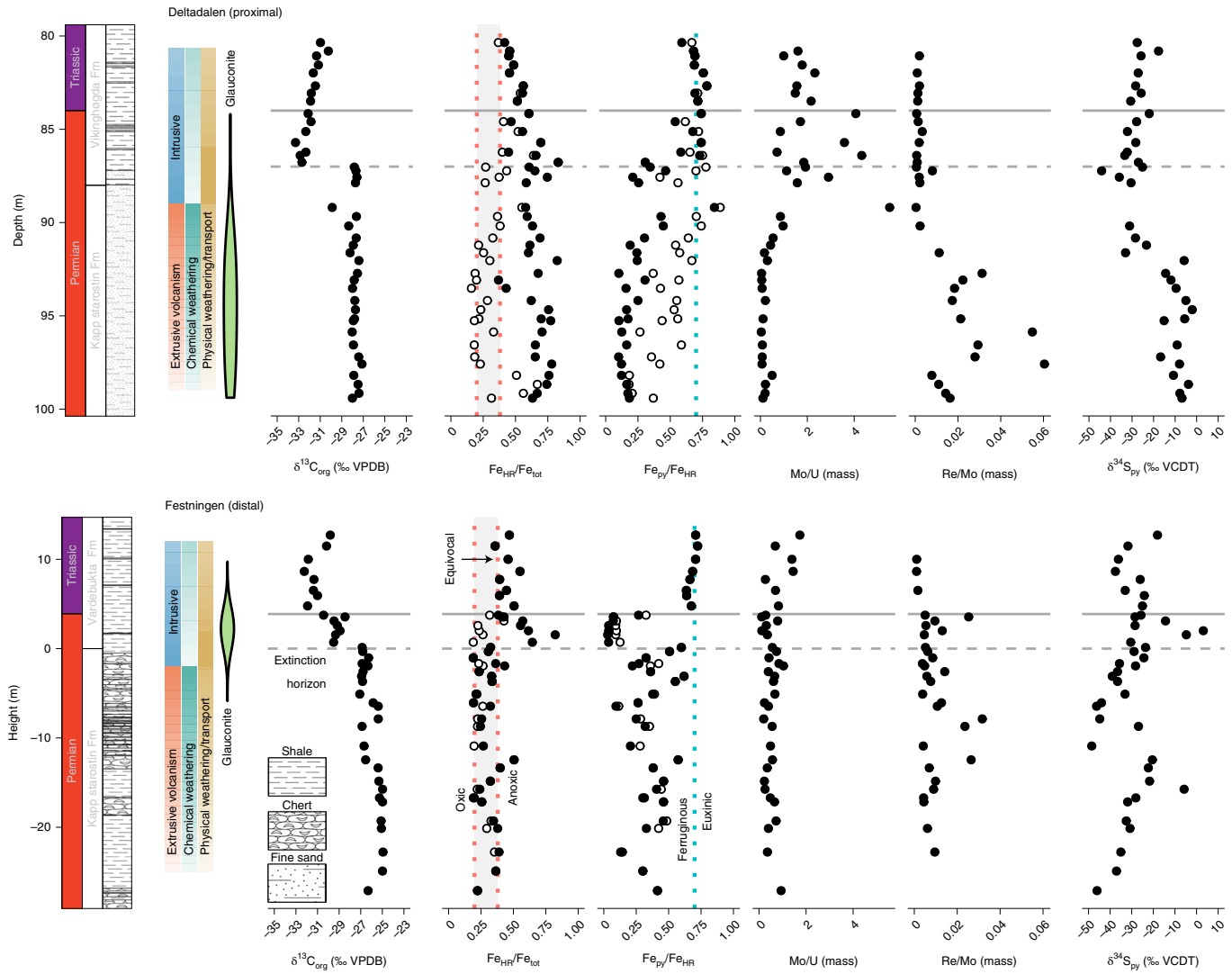

Fig. 2 | Stratigraphic plot of $\delta^{13}C_{org}$, Fe speciation, Mo/U, Re/Mo and $\delta^{34}S_{py}$ for the Festningen outcrop and Deltadalen core. The boundaries (vertical dotted lines) for oxic, anoxic, ferruginous (Fe(II)-rich) and euxinic (H_2S-rich) water-column conditions were calibrated in modern and ancient aquatic environments (see text for sources). Iron speciation (Fe_{py}/Fe_{HR}*, Fe_{HR}/Fe_{tot}*) corrected for excess Fe_{PRS} (excess Fe_{PRS} = (measured Fe_{PRS}/Fe_{tot} − baseline Fe_{PRS}/Fe_{tot}) × Fe_{tot} if measured Fe_{PRS}/Fe_{tot} > baseline Fe_{PRS}/Fe_{tot}) is shown as black circles; uncorrected values are shown as open circles (see section 7.2 of the Supplementary Information). Subscripts of isotope ratios: org, organic carbon; py, pyrite. $Fe_{HR} = Fe_{carb}$ (iron bound to carbonate) + Fe_{ox} (iron bound to Fe oxy(hydr)oxides) + Fe_{mag} (iron bound as magnetite) + Fe_{py}. Reproducibility for Fe_{py} and Fe_{HR} is better than 5% and 9% relative standard deviations (RSDs), better than 8% RSD for total elemental concentrations, and better than 0.1‰ and 0.9‰ s.d. for $\delta^{13}C_{org}$ and $\delta^{34}S_{py}$. Horizontal dashed grey line, extinction event; solid grey line, P–Tr boundary. Details on lithology and stratigraphy in Supplementary Fig. 2 and sections 2 and 3 of the Supplementary Information. VPDB, Vienna PeeDee Belemnite; VCDT, Vienna Canyon Diablo Troilite.

water column in proximal settings at the extinction boundary and into the Early Triassic[33,36]

The sponge spiculite chert of the Kapp Starostin Formation at Festningen (distal) is marked by Fe_{HR}/Fe_{tot}* values in the equivocal zone, as well as low Mo/U and generally low Re/Mo (Fig. 2). These vast sponge meadows are consistent with a well-oxygenated water column[30], whereas infrequent peaks in Re/Mo may indicate occasional dysoxic conditions. A pronounced peak in non-sulfidized iron, coincident with enrichments in Fe_{HR}, the precipitation of glauconite, muted Re/Mo enrichments and bioturbation intensity, occurs at the extinction horizon in the basal Vardebukta Formation (Fig. 2 and Supplementary Fig. 2), suggesting the development of dysoxic and/or ferruginous conditions in the water column. Enrichments in Fe_{HR} persist across the P–Tr boundary at ~5 m above the base of the Vardebukta Formation, with elevated Fe_{py}/Fe_{HR}*, moderate enrichments in Mo relative to U (Fig. 2), the cessation of bioturbation (Supplementary Fig. 2) and Mo_{EF}/U_{EF} that are comparable to normal oxic marine settings (Fig. 3). Together, this implies the probable development of water-column euxinia, but relatively low levels of Mo drawdown imply either intermittent or weakly sulfidic conditions in this more distal setting[45].

The spatio-temporal variability in water-column redox implies the existence of dysoxic conditions on the shallow shelf before the extinction (Fig. 2). Subsequently, at the extinction horizon, euxinic conditions developed at the shallowest location (Deltadalen), and dysoxic to ferruginous conditions expanded into more distal shelf settings (Festningen). This was followed by the expansion of anoxia across the shelf, with euxinic conditions becoming more widespread in the post-extinction Early Triassic. The S isotope composition of pyrite provides additional support for this redox reconstruction.

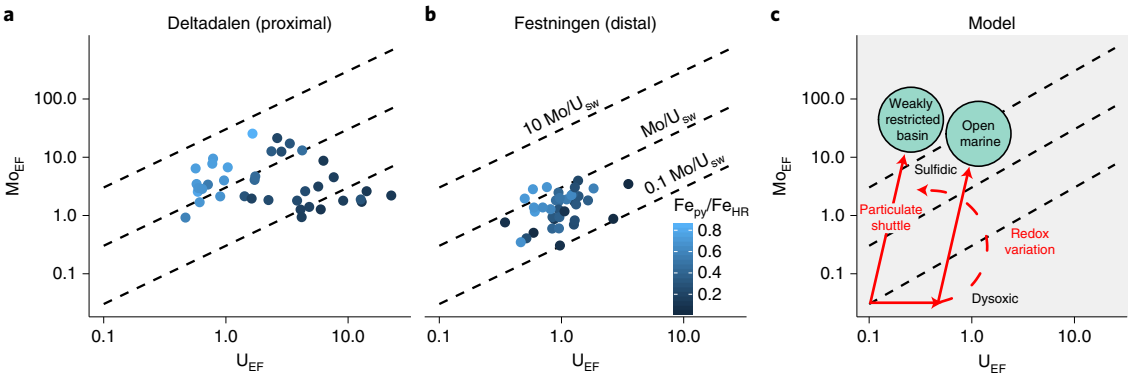

Fig. 3 | Crossplots of Mo/U covariation. Mo and U are given as enrichment factors (EF = [element/Al]$_{sample}$/[element/Al]$_{AV}$, where AV represents average shale[51]) on a log$_{10}$-scale. The black dashed lines represent seawater Mo/U mass ratios for modern environments: high (sulfidic Cariaco Basin), moderate (non-sulfidic open marine) and low (restricted, sulfidic Black Sea)[33]. **a**–**c**, The panels present the data of Deltadalen (**a**), Festningen (**b**) and a conceptual model to explain the enrichment patterns and changes in sedimentary Mo_{EF} and U_{EF} at both sites in relation to hydrographic and redox conditions (**c**)[33]. The solid red lines denoted as 'particulate shuttle' show systematics underlain by a fluctuating chemocline, whereas 'redox variation' pertains to the evolution of water mass chemistry. Note that the red dashed line sketches the trajectory of the open-marine conditions of Deltadalen from dysoxic (low Mo/high U) to euxinic (high Mo/low U).

Generally low and quite variable pyrite $\delta^{34}S$ values ($-32.7 \pm 9.9‰$) before the extinction horizon at the more distal locality (Fig. 2) are consistent with microbial sulfate reduction in sediments deposited beneath an oxic water column[46]. By contrast, high $\delta^{34}S_{py}$ where glauconite is prevalent, both in the lower section of the more-proximal locality ($-16.7 \pm 12.1‰$) and just above the extinction horizon at the more distal locality ($-16.8 \pm 15.1‰$), suggests more-complete consumption of sulfate, possibly linked to temporal and spatial variability in sulfate concentrations across the transect. Particularly in the case of the distal glauconite-rich horizon, relatively high $\delta^{34}S_{py}$ may be due to considerable drawdown of the continental sulfate flux under euxinic conditions on the more-proximal shelf. However, under euxinic conditions at both sites, $\delta^{34}S_{py}$ values cluster around a narrow range ($-27.8 \pm 5.4‰$), which is consistent with the narrow range commonly found in modern and ancient euxinic settings[46,47].

We use our phosphorus data to test two scenarios that are compatible with redox change at the extinction horizon. First, the Fe_{HR} flux from the continent may have dropped (Fig. 2) proportional to the sulfate influx with the switch to deforestation, soil erosion and increased physical weathering[12,15,16,19]. Alternatively, an increase in C_{org} availability (Fig. 4) under eutrophic conditions on the shelf may have increased the production of H_2S, thus overwhelming the continental supply of Fe_{HR}. Both of these scenarios would initially promote enhanced production of sulfide on the more-proximal continental shelf.

Phosphorus recycling and the spread of anoxia

To assess the potential role of phosphorus in driving our proposed redox structure, we quantified different phosphorus-bearing phases (Methods), specifically Fe (oxyhydr)oxide-bound P (P_{Fe}), biogenic and authigenic apatite (P_{aut}), P_{org} and crystalline detrital phases (P_{det})[25]. While detrital P is generally considered unreactive in the water column and during early diagenesis, the remaining phases comprise a 'reactive' P pool (P_{reac}). However, Fe(III)-rich sheet silicates (for example, glauconite) can also effectively trap phosphate[48], which is extracted as part of the P_{det} pool (Supplementary Fig. 7 and section 7.3 of the Supplementary Information).

Before the extinction at Deltadalen (proximal), P_{tot}/Al is considerably enriched relative to average marine shale (Fig. 4). This suggests an effective drawdown mechanism from a water column that was rich in phosphate. Furthermore, although preferential release from organic matter occurred during diagenesis (C_{org}/P_{org} > the molar Redfield ratio of 106/1), low C_{org}/P_{reac} ratios ($\ll$106/1) combined with high P_{tot}/Al suggest effective sequestration of P in the sediment, with no evidence for extensive recycling. To explain these observations, we invoke a high initial weathering influx of phosphorus to the proximal shelf associated with initial emplacement of the Siberian Traps before the extinction[18], which enhanced productivity and C_{org} remineralization in the water column, leading to the development of dysoxic conditions (Fig. 5). However, the extent and intensity of deoxygenation was limited by effective drawdown of P to the sediments in association with both C_{org} and the high weathering influx of Fe (oxyhydr)oxide minerals, and with long-term retention in CFA and glauconite (Supplementary Fig. 7).

These factors then controlled the geochemistry before the extinction at Festningen (distal), where P_{tot}/Al ratios are close to average shale, C_{org}/P_{org} ratios are elevated relative to the Redfield ratio and C_{org}/P_{reac} ratios scatter close to the Redfield ratio (Fig. 4). This suggests that the high initial weathering influx of P was efficiently sequestered in more-proximal settings, thus limiting the spatial extent of dysoxic conditions. Furthermore, while P was released from organic matter during microbial respiration ($C_{org}/P_{org} > 106/1$), there is little evidence for a high sustained flux back to the water column ($C_{org}/P_{reac} \approx 106$), consistent with the expected behaviour of P in sediments deposited beneath an oxic water column[27,28].

At the extinction horizon, P_{tot}/Al ratios decrease to average shale values at Deltadalen (proximal), and both C_{org}/P_{org} and C_{org}/P_{reac} ratios increase considerably to values that exceed the Redfield ratio (Fig. 4). This suggests that the development of euxinia fuelled efficient release of P from both C_{org} and Fe (oxyhydr)oxides, and a positive productivity feedback was promoted via enhanced P recycling. The initial driver of euxinia is more difficult to ascertain but was probably related to the change to a chemical weathering-limited denudation regime[19] (Fig. 2), thereby decreasing the land-derived influx of Fe_{HR}. This led to a tipping point whereby a relative excess of dissolved sulfate over Fe_{HR} promoted the development of euxinia[36]. As discussed earlier, an increase in eutrophication driven by an enhanced nutrient influx may also have promoted sulfide production. However, this seems a less likely explanation for the initial driver of euxinia given the already high input of P (Fig. 4).

In glauconite-rich sediments immediately above the extinction horizon at Festningen (distal), there is an initial peak in P_{tot}/Al in association with the development of dysoxic and/or ferruginous conditions. Here, our detailed P speciation analyses suggest that, as with the glauconite-rich horizon in the proximal locality, P was trapped in the sediment in association with CFA and glauconite (Supplementary Fig. 7). The high P content of this horizon probably

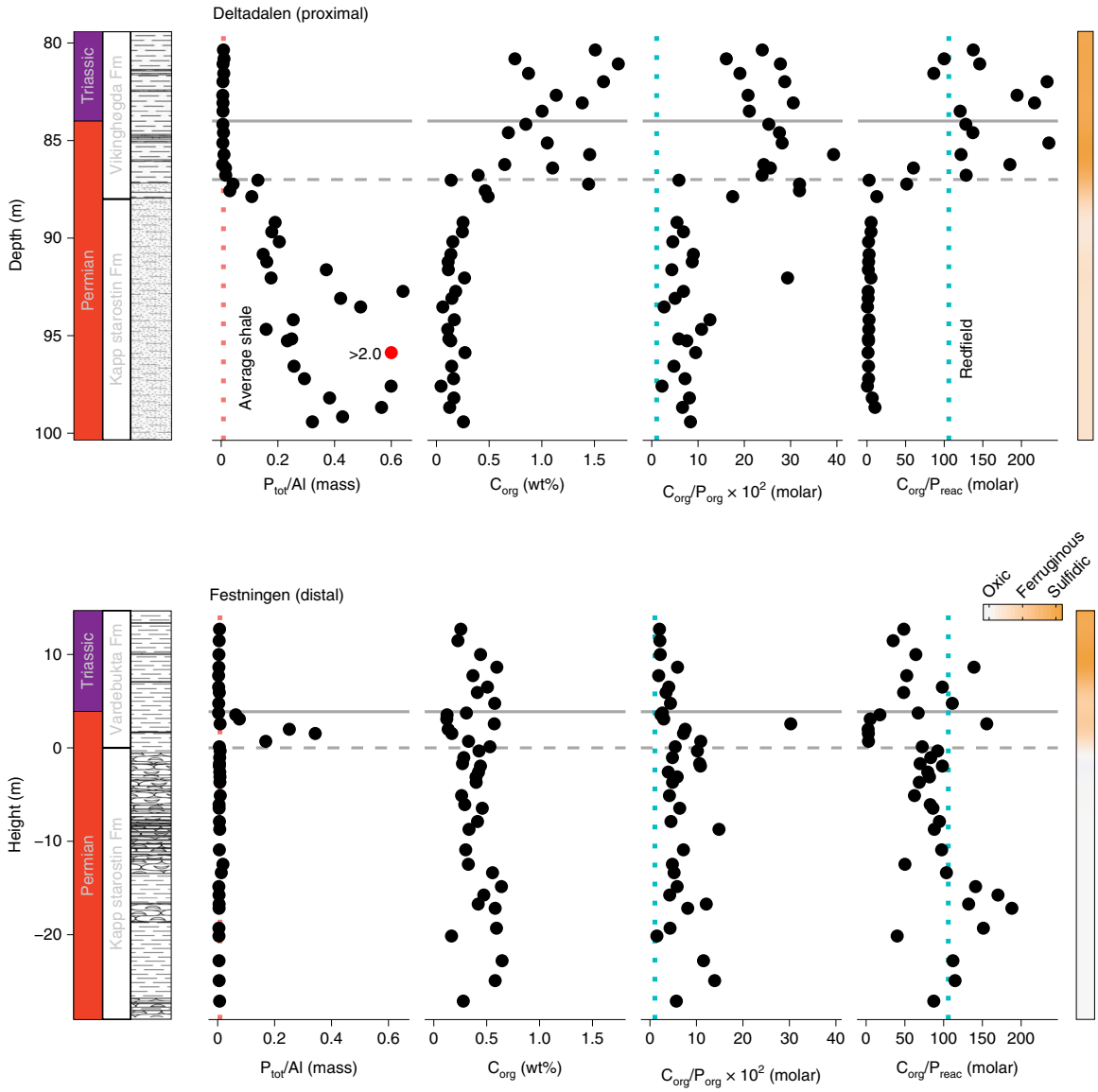

Fig. 4 | Stratigraphic distribution of P_{tot}/Al, C_{org}, C_{org}/P_{org} and C_{org}/P_{reac} ratios. The threshold of P_{tot}/Al (mass ratio of 0.008; vertical dotted red line) is the average shale reference value[51], whereas the C/P molar ratio of 106/1 denotes the Redfield ratio (vertical dotted blue line), and the red circle represents an outlier (P_{tot}/Al > 2.0). C_{org}, organic carbon; P_{reac}, reactive phosphorus ($P_{org} + P_{aut} + P_{Fe}$). External reproducibility for total P and Al is better than 8% RSD, for C_{org} is better than 10% RSD, and for the different P phases is better than 23% RSD. Horizontal dashed grey line, extinction event; solid grey line, Permian–Triassic boundary. Details on lithology and stratigraphy in Supplementary Fig. 2 and sections 2 and 3 of the Supplementary Information.

occurred due to drawdown of P that was recycled under euxinic conditions in more-proximal settings, suggesting the operation of a redox-controlled nutrient shuttle across the shelf. This nutrient shuttle then drove the development of marine euxinia to its maximum extent in the aftermath of the mass extinction (Fig. 5), where wind/density-driven water circulation on the shelf would support upward transport of recycled P and thus sustained deoxygenation[11]. At Festningen, however, the development of only weak or intermittent euxinia after the P–Tr boundary restricted the extent of P recycling to the water column ($C_{org}/P_{reac} \approx 106/1$; Fig. 4), which effectively constrained the maximum spatial extent of euxinia.

Implications for extinction selectivity

This P-driven biogeochemical cascade is synchronous with independent proxy records for the global-scale spread of anoxic water masses[5,7], and it was this that initiated the main marine extinction pulse. The P-driven control on the extent of initial deoxygenation and subsequent euxinia promoted life-viable environments in the deep marine realm, thereby shaping the ecosystems of the surviving biota. On the basis of the benthos that survived the end-Permian mass extinction at Deltadalen, a planktotrophic larval stage[49] (section 7.1 of the Supplementary Information) and a high tolerance to low-oxygen conditions are important traits. These benthic species could rapidly disperse over large distances, thus increasing the chance of survival in habitable locations.

In accordance with theoretical ecological models[50], environmental deterioration of the marine realm began before the extinction pulse. The initial development of dysoxic/anoxic water masses, which were preferentially situated in shallow marine environments in the Boreal region[20], may thus be regarded as a prelude to the impending mass extinction. Our redox model also resolves the apparent conflict between the timing of magmatic activity[18], enhanced weathering[16] and the main extinction pulse. The sum of these changes in marine redox conditions across large stretches of

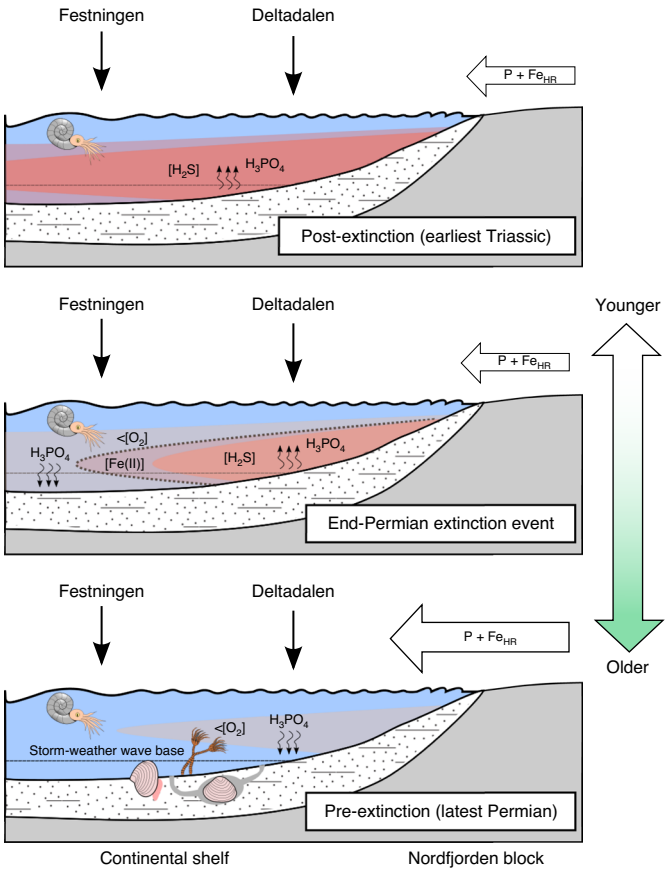

Fig. 5 | Conceptual model of the development of water-column redox conditions. In the latest Permian, the inner shelf was dysoxic (demarcated with <[O_2]), and large amounts of reactive P accumulated, whereas the outer shelf harboured a thriving ecosystem (here depicted as crinoids and molluscs, but which are not representative of the actual fossil assemblages). During the end-Permian mass extinction, euxinia (demarcated with [H_2S]) developed on the inner shelf, whereas the outer shelf environment became dysoxic/ferruginous (demarcated with [Fe(II)]). Under these conditions, P was remobilized as dissolved P (demarcated with H_3PO_4) from the inner shelf, invigorating productivity (and thus oxygen depletion), and dissolved P was recycled to the outer shelf and initially deposited through uptake by Fe (oxyhydr)oxide particles settling on the seabed. After the extinction, euxinic conditions became more prevalent across the shelf, initiated and maintained by recycling of P.

the shelf, which harboured the majority of the Palaeozoic biodiversity[2], appears to have been detrimental to many life forms at the end of the Permian.

Online content

Any methods, additional references, Nature Research reporting summaries, source data, extended data, supplementary information, acknowledgements, peer review information; details of author contributions and competing interests; and statements of data and code availability are available at https://doi.org/10.1038/s41561-020-0622-1.

Received: 30 October 2019; Accepted: 9 July 2020;
Published online: 17 August 2020

References

1. Burgess, S. D., Bowring, S. & Shen, S.-Z. High-precision timeline for Earth's most severe extinction. *Proc. Natl Acad. Sci. USA* **111**, 3316–3321 (2014).
2. Wignall, P. B. & Twitchett, R. J. Oceanic anoxia and the end Permian mass extinction. *Science* **272**, 1155–1158 (1996).
3. Cao, C. et al. Biogeochemical evidence for euxinic oceans and ecological disturbance presaging the end-Permian mass extinction event. *Earth Planet. Sci. Lett.* **281**, 188–201 (2009).
4. Nabbefeld, B. et al. An integrated biomarker, isotopic and palaeoenvironmental study through the Late Permian event at Lusitaniadalen, Spitsbergen. *Earth Planet. Sci. Lett.* **291**, 84–96 (2010).
5. Brennecka, G. A., Herrmann, A. D., Anbar, A. D. & Algeo, T. J. Rapid expansion of oceanic anoxia immediately before the end-Permian mass extinction. *Proc. Natl Acad. Sci. USA* **108**, 17631–17634 (2011).
6. Dustira, A. M. et al. Gradual onset of anoxia across the Permian–Triassic boundary in Svalbard, Norway. *Palaeogeogr. Palaeoclimatol. Palaeoecol.* **374**, 303–313 (2013).
7. Schobben, M. et al. Flourishing ocean drives the end-Permian marine mass extinction. *Proc. Natl Acad. Sci. USA* **112**, 10298–10303 (2015).
8. Stanley, S. M. Estimates of the magnitudes of major marine mass extinctions in Earth history. *Proc. Natl Acad. Sci. USA* **113**, E6325–E6334 (2016).
9. Kiehl, J. T. & Shields, C. A. Climate simulation of the latest Permian: implications for mass extinction. *Geology* **33**, 757–760 (2005).
10. Hotinski, R. M., Bice, K. L., Kump, L. R., Najjar, R. G. & Arthur, M. A. Ocean stagnation and end-Permian anoxia. *Geology* **29**, 7–10 (2001).
11. Meyer, K., Kump, L. & Ridgwell, A. Biogeochemical controls on photic-zone euxinia during the end-Permian mass extinction. *Geology* **36**, 747–750 (2008).
12. Algeo, T. J. & Twitchett, R. J. Anomalous Early Triassic sediment fluxes due to elevated weathering rates and their biological consequences. *Geology* **38**, 1023–1026 (2010).
13. Shen, J. et al. Marine productivity changes during the end-Permian crisis and Early Triassic recovery. *Earth-Sci. Rev.* **149**, 136–162 (2015).
14. Tyrrell, T. The relative influences of nitrogen and phosphorus on oceanic primary production. *Nature* **400**, 525–531 (1999).
15. Sephton, M. A. et al. Catastrophic soil erosion during the end-Permian biotic crisis. *Geology* **33**, 941–944 (2005).
16. Sun, H. et al. Rapid enhancement of chemical weathering recorded by extremely light seawater lithium isotopes at the Permian–Triassic boundary. *Proc. Natl Acad. Sci. USA* **115**, 3782–3787 (2018).
17. Visscher, H. et al. Environmental mutagenesis during the end-Permian ecological crisis. *Proc. Natl Acad. Sci. USA* **101**, 12952–12956 (2004).
18. Burgess, S. D., Muirhead, J. D. & Bowring, S. A. Initial pulse of Siberian Traps sills as the trigger of the end-Permian mass extinction. *Nat. Commun.* **8**, 164 (2017).
19. Ward, P. D., Montgomery, D. R. & Smith, R. Altered river morphology in South Africa related to the Permian–Triassic extinction. *Science* **289**, 1740–1743 (2000).
20. Algeo, T. et al. Evidence for a diachronous late Permian marine crisis from the Canadian Arctic region. *Geol. Soc. Am. Bull.* **124**, 1424–1448 (2012).
21. Froelich, P. N. et al. Early oxidation of organic matter in pelagic sediments of the eastern equatorial: suboxic diagenesis. *Geochim. Cosmochim. Acta* **43**, 1075–1090 (1979).
22. Krom, M. D. & Berner, R. A. The diagenesis of phosphorus in a nearshore marine sediment. *Geochim. Cosmochim. Acta* **45**, 207–216 (1981).
23. Slomp, C. P., Van Der Gaast, S. J. & Van Raaphorst, W. Phosphorus binding by poorly crystalline iron oxides in North Sea sediments. *Mar. Chem.* **52**, 55–73 (1996).
24. Schenau, S. J. & De Lange, G. J. A novel chemical method to quantify fish debris in marine sediments. *Limnol. Oceanogr.* **45**, 963–971 (2000).
25. Ruttenberg, K. C. Development of a sequential extraction method for different forms of phosphorus in marine sediments. *Limnol. Oceanogr.* **37**, 1460–1482 (1992).
26. Egger, M., Jilbert, T., Behrends, T., Rivard, C. & Slomp, C. P. Vivianite is a major sink for phosphorus in methanogenic coastal surface sediments. *Geochim. Cosmochim. Acta* **169**, 217–235 (2015).
27. Cappellen, P. V. & Ingall, E. D. Redox stabilization of the atmosphere and oceans by phosphorus-limited marine productivity. *Science* **271**, 493–496 (1996).
28. Algeo, T. J. & Ingall, E. Sedimentary C_{org}:P ratios, paleocean ventilation, and Phanerozoic atmospheric pO_2. *Palaeogeogr. Palaeoclimatol. Palaeoecol.* **256**, 130–155 (2007).
29. Harland, W. *The Geology of Svalbard* (Geological Society, 1997).
30. Blomeier, D., Dustira, A. M., Forke, H. & Scheibner, C. Facies analysis and depositional environments of a storm-dominated, temperate to cold, mixed siliceous–carbonate ramp: the Permian Kapp Starostin Formation in NE Svalbard. *Nor. J. Geol.* **93**, 75–93 (2013).
31. Zuchuat, V. et al. A new high-resolution stratigraphic and palaeoenvironmental record spanning the end-Permian mass extinction and its aftermath in central Spitsbergen, Svalbard. *Palaeogeogr. Palaeoclimatol. Palaeoecol.* **554**, 109732 (2020).
32. Poulton, S. W. & Canfield, D. E. Development of a sequential extraction procedure for iron: implications for iron partitioning in continentally derived particulates. *Chem. Geol.* **214**, 209–221 (2005).

33. Algeo, T. & Tribovillard, N. Environmental analysis of paleoceanographic systems based on molybdenum–uranium covariation. *Chem. Geol.* **268**, 211–225 (2009).
34. Raiswell, R. & Canfield, D. E. Sources of iron for pyrite formation in marine sediments. *Am. J. Sci.* **298**, 219–245 (1998).
35. Poulton, S. W. & Raiswell, R. The low-temperature geochemical cycle of iron: from continental fluxes to marine sediment deposition. *Am. J. Sci.* **302**, 774–805 (2002).
36. Poulton, S. W. & Canfield, D. E. Ferruginous conditions: a dominant feature of the ocean through Earth's history. *Elements* **7**, 107–112 (2011).
37. Lyons, T. W. & Severmann, S. A critical look at iron paleoredox proxies: new insights from modern euxinic marine basins. *Geochim. Cosmochim. Acta* **70**, 5698–5722 (2006).
38. Poulton, S. W., Fralick, P. W. & Canfield, D. E. Spatial variability in oceanic redox structure 1.8 billion years ago. *Nat. Geosci.* **3**, 486–490 (2010).
39. Doyle, K. A., Poulton, S. W., Newton, R. J., Podkovyrov, V. N. & Bekker, A. Shallow water anoxia in the Mesoproterozoic ocean: evidence from the Bashkir Meganticlinorium, Southern Urals. *Precambrian Res.* **317**, 196–210 (2018).
40. Kendall, B. et al. Pervasive oxygenation along late Archaean ocean margins. *Nat. Geosci.* **3**, 647–652 (2010).
41. Chafetz, H. S. & Reid, A. Syndepositional shallow-water precipitation of glauconitic minerals. *Sediment. Geol.* **136**, 29–42 (2000).
42. Peters, S. E. & Gaines, R. R. Formation of the 'Great Unconformity' as a trigger for the Cambrian explosion. *Nature* **484**, 363–366 (2012).
43. Manwell, C. Oxygen equilibrium of brachiopod *Lingula* hemerythrin. *Science* **132**, 550–551 (1960).
44. Peng, Y., Shi, G. R., Gao, Y., He, W. & Shen, S. How and why did the Lingulidae (Brachiopoda) not only survive the end-Permian mass extinction but also thrive in its aftermath? *Palaeogeogr. Palaeoclimatol. Palaeoecol.* **252**, 118–131 (2007).
45. Scott, C. & Lyons, T. W. Contrasting molybdenum cycling and isotopic properties in euxinic versus non-euxinic sediments and sedimentary rocks: refining the paleoproxies. *Chem. Geol.* **324-325**, 19–27 (2012).
46. Lyons, T. W. Sulfur isotopic trends and pathways of iron sulfide formation in upper Holocene sediments of the anoxic Black Sea. *Geochim. Cosmochim. Acta* **61**, 3367–3382 (1997).
47. Shen, Y., Canfield, D. E. & Knoll, A. H. Middle proterozoic ocean chemistry: evidence from the McArthur Basin, Northern Australia. *Am. J. Sci.* **302**, 81–109 (2002).
48. Borgnino, L., Avena, M. & De Pauli, C. Synthesis and characterization of Fe(III)-montmorillonites for phosphate adsorption. *Colloids Surf. A* **341**, 46–52 (2009).
49. Foster, W. J., Danise, S. & Twitchett, R. J. A silicified Early Triassic marine assemblage from Svalbard. *J. Syst. Palaeontol.* **15**, 851–877 (2017).
50. Barnosky, A. D. et al. Approaching a state shift in Earth's biosphere. *Nature* **486**, 52–58 (2012).
51. Wedepohl, K. H. in *Metals and Their Compounds in the Environment* (ed. Merian, E.) 3–17 (Verlag Chemie, 1991).

Methods

C_{org} content and carbon isotopes. Carbonate was removed by treating the sample with 2 M HCl. The residues were repeatedly washed with Milli-Q water and dried at 40 °C. The de-carbonated samples were analysed for total organic carbon (TOC = C_{org}) content and associated carbon isotopic composition using an Elementar Pyrocube elemental analyser linked to an Isoprime mass spectrometer following a standard protocol. Details regarding the reproducibility of the carbon isotope measurements and an extended protocol are included in section 6.2 of the Supplementary Information.

Bulk element content. Whole-rock major (Fe, P, Al) and minor (Mo, U, Re) elements were obtained by dissolving ashed samples (550 °C overnight) with HNO_3–HF–$HClO_4$ followed by inductively coupled plasma optical emission spectrometry (ICP-OES). The precision of elemental analysis was monitored by analysing certified standards, and repeated measurement yielded relative standard deviations that are better than 8% for all elements (section 6.1 of the Supplementary Information and Supplementary Table 1).

Sequential Fe and P extractions. A standard sequential Fe extraction was followed[32]. A sodium acetate solution at pH 4.5 for 48 h at 50 °C was used to extract Fe_{carb}, followed by a 2-h, room-temperature extraction with sodium dithionite solution at pH 4.8 to obtain Fe_{ox}. An extraction with ammonium oxalate for 6 h at room temperature was then applied to yield Fe_{mag}. Iron from Fe_{PRS} was dissolved using concentrated, boiling HCl for 1 min[32]. Iron concentrations in the extraction solutions were measured via atomic absorption spectrometry. Phosphorus phases were extracted via a revised SEDEX scheme for ancient rocks[25,52]. Poorly crystalline Fe (oxyhydr)oxides (P_{Fe1}) were extracted with a sodium dithionite solution (buffered with bicarbonate to pH of 7.6) for 8 h at room temperature; P_{aut} was extracted with a sodium acetate solution at pH 4 for 6 h at room temperature; P_{det} was extracted with a 10% HCl solution for 16 h at room temperature; P_{mag} was extracted with an ammonium oxalate solution for 6 h at room temperature; P_{Fe2} (more crystalline Fe (oxyhydr)oxides) was extracted with a sodium dithionite solution (buffered with citrate to a pH of 4.8) for 8 h at room temperature, and finally, the residue was ashed (550 °C for 2 h) and reacted with 10% HCl solution for 16 h at room temperature to liberate P_{org}. The sum of $P_{Fe1} + P_{Fe2} + P_{mag}$ gives P_{Fe}. The P content of the various extracts was determined via either the molybdate blue method[25] or inductively coupled plasma optical emission spectrometry (in the case of P_{Fe1}, P_{Fe2} and P_{mag}). The precision of the various Fe and P phase measurements as well as the extended protocols are reported in section 6.1 of the Supplementary Information and Supplementary Tables 2 and 3.

Pyrite content and sulfur isotopes. The S_{py} was measured via the chromium reduction method[53]. This method liberates H_2S, which is subsequently trapped as silver sulfide (Ag_2S). The Fe_{py} was determined stochiometrically from the weight of the Ag_2S recovered. The Ag_2S was analysed for S isotope composition using an Elementar Pyrocube linked to an Isoprime mass spectrometer (see section 6.2 of the Supplementary Information for reproducibility of S isotope measurements and an extended protocol).

Data availability

P.B.W. (P.B.Wignall@leeds.ac.uk) and S.P. (planke@vbpr.no) should be consulted for material requests of Festningen and Deltadalen, respectively. The raw and processed geochemical data that support the findings of this study are available under Zenodo: https://doi.org/10.5281/zenodo3878094.

Code availability

The R Markdown files to reproduce the data analysis as well as generate the accompanying data figures and the main and supplementary information texts can be found under Zenodo: https://doi.org/10.5281/zenodo.3878094.

References

52. Thompson, J. et al. Development of a modified SEDEX phosphorus speciation method for ancient rocks and modern iron-rich sediments. *Chem. Geol.* **524**, 383–393 (2019).
53. Canfield, D. E., Raiswell, R., Westrich, J. T., Reaves, C. M. & Berner, R. A. The use of chromium reduction in the analysis of reduced inorganic sulfur in sediments and shales. *Chem. Geol.* **54**, 149–155 (1986).

Acknowledgements

M.S. was funded by a DFG Research Fellowship (SCHO 1689/1–1). S.W.P. acknowledges support from a Royal Society Wolfson Research Merit Award and a Leverhulme Research Fellowship. D.P.G.B. acknowledges funding from the Natural Environment Research Council (NE/J01799X/1) as do P.B.W. and R.J.N. (NE/P013724/1). H.H.S. and S.P. acknowledge support from the Norwegian Research Council by Centres of Excellence funding to CEED (project number 223272), and Lundin Petroleum, Arctic Drilling AS and Store Norske Spitsbergen Kulkompani for funding, drilling and support related to the Deltadalen core.

Author contributions

The study was designed by M.S., R.J.N., P.B.W. and S.W.P. Samples were collected by V.Z., A.R.N.S., H.H.S., S.P., P.B.W. and D.P.G.B. Palaeontological data acquisition was performed by W.J.F., M.S., P.B.W. and D.P.G.B. Geochemical analyses were performed by M.S., F.M. and R.J.N. M.S. and S.W.P. interpreted data. M.S. led the writing of the manuscript with contributions from all co-authors.

Competing interests

The authors declare no competing interests.

Additional information

Supplementary information is available for this paper at https://doi.org/10.1038/s41561-020-0622-1.

Correspondence and requests for materials should be addressed to M.S.

Peer review information Primary Handling Editor: James Super.

Reprints and permissions information is available at www.nature.com/reprints.